

Numerical study of thermo-mechanical effects on the viscous damage behavior of rock salt caverns

Zhu, C.

Bureau of Economic Geology, The University of Texas at Austin, Austin, Texas

Shen, X. and Arson, C.

School of Civil and Environmental Engineering, Georgia Institute of Technology, Atlanta, Georgia

Pouya, A.

Laboratoire Navier (IFSTTAR, CNRS, ENPC), Paris-Est University, Champs sur Marne, France

ABSTRACT: Underground cavities in rock salt have received increased attention for the storage of oil, gas, and compressed air energy. In this study, the transition between secondary and tertiary creep in salt is determined by a micro-macro model: The initiation of grain breakage is correlated with the acceleration of viscoplastic deformation rate and with the initiation of damage at the macroscopic scale. Salt stiffness decreases when macroscopic damage increases, which allows predicting the evolution of the damage zone around salt caverns used for geological storage. After implementing the phenomenological model into the Finite Element Method (FEM) program POROFIS, two thermo-mechanical coupled stress paths are simulated to analyze stress concentrations and viscous damage around a 650-m-deep cavern in axisymmetric conditions. Numerical results indicate that, despite the pressurization or depressurization-induced temperature variation, internal gas temperature always tends to approach the primary surrounding rock mass value. The viscous deformation induced by thermo-mechanical couplings significantly affects the original stress field at the cavern wall and induces high damage at the most concave sections of the cavern. Results reveal the significant influences of idle time, gas pressure range, and injection and withdrawal cycles on stress, strain and temperature distributions in the vicinity of the cavern. More analyses are needed to confirm the influence of thermo-mechanical cycles of pressurization and depressurization, and to design long-term cavern operations.

1. INTRODUCTION

Salt rock is a favorable hosting material for geological storage, including the storage of hydrogen, oil and gas, as well as Compressed Air Energy Storage (CAES). The design and performance assessment of such facilities require a fundamental understanding of the complex time-dependent behavior of salt, which depends on both salt properties and environmental factors (Carter and Hansen, 1983). Increasing deviatoric stress or decreasing confining pressure induces increasing steady-state strain rate in salt (Yang et al., 1999). The presence of brine at grain boundaries considerably influences the halite rheology and deformation (Urai et al., 1986). Temperature is also a crucial component for rock deformation around nuclear waste disposals (Senseny et al., 1992; Zheng et al., 2016) and CAES (Leuger et al., 2012).

In salt caverns used for geological storage, high stresses near the cavity wall results in significant viscoplastic response of salt. Usually, the damage process is associated with a crack-induced volumetric deformation,

captured by a dilatancy boundary. Phenomenological models based on the dilatancy boundary do not account for stiffness changes and could not predict damage-induced anisotropy and strength reduction associated with the opening of microcracks or microvoids, which has been observed during salt creep and also in other brittle solids. Damage-induced relaxation was accounted for in the constitutive model proposed by Haupt (1991). The multi-mechanism deformation model, first proposed by Munson and Dawson (1984), was further extended by Chan et al. (1992) to study creep-induced damage. A restrictions-based thermodynamic framework was formulated by Chen et al. (1997) to capture the transition between secondary and tertiary creep. However, these creep-damage-coupled models resort to a larger number of constitutive parameters and ignore the correlation between macroscopic deformation rate and the governing microscopic mechanisms.

In addition, gas temperature changes need to be considered when cavern are subjected to cycles of pressurization and depressurization instead of being used for long-term storage. Compressed gas is quickly

withdrawn, going from high to relatively low pressure. As a result, the gas temperature tends to decrease and reach a lower level than in the primary surrounding rock mass (Leuger et al., 2012). Thermo-mechanical stresses may exceed the (low) tensile strength of salt rock and cause tensile failure at the vicinity of the cavern. Therefore, viscous deformation and damage during long-term thermo-mechanical coupled pressurization and depressurization processes in salt caverns are great concerns to engineers and researchers.

This study aims to gain a fundamental understanding of the evolution of viscous damage in salt caverns subject to typical thermo-mechanical storage conditions. Section 2 explains the framework of the phenomenological model that captures the viscous deformation and induced damage in salt. Section 3 explains how the Finite Element (FE) model was configured and how the modeling parameters were determined. Section 4 presents the results of FE simulations of two loading paths involving different pressurization and depressurization processes. Viscous deformation and damage development around the salt cavern are discussed.

2. PHENOMENOLOGICAL MODEL

2.1. Rheology of salt

The total mechanical deformation rate $\dot{\boldsymbol{\varepsilon}}$ can be decomposed into elastic and viscoplastic contributions as

$$\dot{\boldsymbol{\varepsilon}} = \dot{\boldsymbol{\varepsilon}}^e + \dot{\boldsymbol{\varepsilon}}^{vp} \quad (1)$$

in which $\dot{\boldsymbol{\varepsilon}}^e$ is a function of the stress rate, and $\dot{\boldsymbol{\varepsilon}}^{vp}$ is the viscoplastic strain rate. If temperature varies, an additional volumetric strain rate component $\dot{\boldsymbol{\varepsilon}}^t$ resulting from temperature variation is included. The total strain rate is the sum of mechanical and thermal strain rate:

$$\dot{\boldsymbol{\varepsilon}}^t = \alpha_T \dot{T} \boldsymbol{\delta} \quad (2)$$

$$\dot{\boldsymbol{\varepsilon}}^{tot} = \dot{\boldsymbol{\varepsilon}}^e + \dot{\boldsymbol{\varepsilon}}^{vp} + \dot{\boldsymbol{\varepsilon}}^t \quad (3)$$

in which α_T is the thermal expansion coefficient, \dot{T} is the temperate change rate, and $\boldsymbol{\delta}$ is the Kronecker delta operator.

In most polycrystalline materials, deformation is mostly driven by slip: All possible slip systems contribute to the viscoplastic strain rate $\dot{\boldsymbol{\varepsilon}}^{vp}$ in a grain, as follows:

$$\dot{\varepsilon}_{ij}^{vp} = \sum \dot{\gamma}^l a_{ij}^l \quad (4)$$

in which $a_{ij}^l = 0.5(m_i^l n_j^l + n_i^l m_j^l)$ denotes the l^{th} slip system of the mono-crystal in global matrix coordinate, \mathbf{m}^l and \mathbf{n}^l are the orthonormal unit vectors defining the slip direction and the normal to the l^{th} slip system, respectively, and $\dot{\gamma}^l$ is the viscoplastic strain rate for the l^{th} slip mechanism.

Salt has a face-centered cubic (FCC) crystal structure. Among the six possible preferential slip planes during grain shear deformation, only two of them are independent. In agreement with experimental observations (e.g., Kalidindi et al., 1992), we assumed a power law for the irreversible shear strain:

$$\dot{\gamma}^l = \gamma_0 h^l \left| \frac{\tau^l}{\tau_0} \right|^n \quad (5)$$

in which γ_0 is a reference strain rate, τ_0 is a reference shear stress and takes an arbitrary value of 1 MPa, τ^l is the local shear stress, n characterizes the sensitivity of the slip rate on stress, and h^l depends on the sign of τ^l ($\tau^l > 0, h^l = 1; \tau^l < 0, h^l = -1$).

2.2. Viscous deformation and damage

We propose a phenomenological model of viscoplastic deformation to account for salt viscous damage. This model captures the transition between secondary and tertiary creep regimes, based on a micro-macro damage criterion. Grain-scale sliding mechanisms contribute to the viscoplastic deformation during the secondary creep. Tertiary creep corresponds to the rapid increase of strain rate with damage as a result of grain breakage.

We resort to the Norton-Hoff law to model secondary creep (Carter and Hansen, 1983):

$$\boldsymbol{\varepsilon}_s^{vp} = \frac{3}{2} A \cdot \exp\left(-\frac{Q}{RT}\right) \left(\frac{\sigma_e}{\sigma_0}\right)^{n_1} \frac{1}{\sigma_e} \mathbf{s} \quad (6)$$

in which A and n_1 are material-dependent parameters, Q is the slip activation energy, R is the universal gas constant, T is the absolute temperature, \mathbf{s} is the deviatoric stress tensor, σ_0 is a reference stress (arbitrarily set equal to 1 MPa), $\sigma_e = \sqrt{3J_2}$ is the equivalent von Mises stress with $J_2 = \frac{s_{ij}s_{ij}}{2}$ representing the second deviatoric stress invariant.

The continuous increase of microstresses due to macroscopic viscoplastic deformation could lead to grain breakage if the grain tensile strength is exceeded. Consequent microstress redistribution may cause higher local stress concentrations, resulting in accelerated viscoplastic deformation and damage propagation (Ma and Haimson, 2016; Pouya et al., 2016), which is known as tertiary creep (Fig. 1). We related the onset of first grain breakage and the progressive opening of microcracks and microvoids to damage initiation and accumulation, respectively.

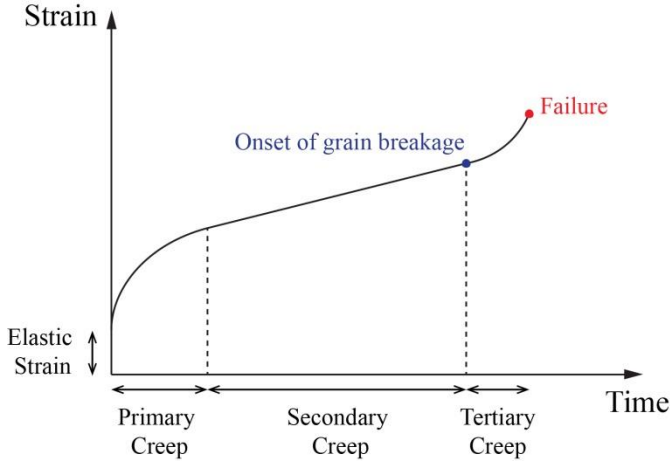


Fig. 1 Creep curve composed of three phases: primary creep, secondary creep and tertiary creep. The onset of grain breakage corresponds to the initiation of tertiary creep.

The tertiary creep deformation law follows a similar form as the secondary (steady state) creep, but captures the accelerated strain rate due to damage evolution:

$$\varepsilon_t^{vp} = \frac{3}{2} B \cdot \exp\left(-\frac{Q}{RT}\right) \left[\frac{\sigma_e}{\sigma_0(1-D_M)}\right]^{n_2} \frac{1}{\sigma_e} \mathbf{s} \quad (7)$$

in which B and n_2 are material-dependent parameters, $\frac{\sigma_e}{1-D_M}$ is the effective stress, and D_M is the damage variable. The damaged material stiffness \mathbf{C}_D can be derived from the initial stiffness \mathbf{C}_0 at the undamaged state:

$$\mathbf{C}_D = (1 - D_M)\mathbf{C}_0 \quad (8)$$

We adopted a damage evolution law that depends on the current viscoplastic deformation state only, which proved to be successful to model cementitious materials. Damage of the deformed material is assumed to remain zero before the deformation reaches a critical viscoplastic value ε_0^{vp} , and then follows an exponentially evolution law:

$$D_M = 1 - e^{-\frac{\varepsilon^{vp} - \varepsilon_0^{vp}}{\chi \varepsilon_0^{vp}}} \quad (9)$$

with the rate of damage expressed as:

$$\dot{D}_M = \frac{1}{\chi \varepsilon_0^{vp}} \|\varepsilon^{vp}\| e^{-\frac{\varepsilon^{vp} - \varepsilon_0^{vp}}{\chi \varepsilon_0^{vp}}} \quad (10)$$

in which ε_0^{vp} corresponds to the onset of tertiary creep, χ characterizes the ductility of the material, with higher χ representing a more ductile behavior of the material.

$\|\varepsilon^{vp}\| = \sqrt{\frac{2}{3} \dot{D}_M D_M}$ is the equivalent von Mises strain.

For a completely broken grain, the damage variable D_M is equal to 1, which means that the grain is a void.

This study concerns the long-term behavior of salt cavern subjected to time-dependent loadings, which requires the determination of a damage criterion from long-term test datasets. Following our previous study (Zhu et al., 2015), we take the damage threshold as a bilinear form:

$$\varepsilon_c^{vp} = 5 \times 10^{-5} \sigma_c - 2 \times 10^{-5} \quad (2 \leq \sigma_c \leq 4.78) \quad (11)$$

$$\varepsilon_c^{vp} = 4 \times 10^{-6} \sigma_c + 2 \times 10^{-4} \quad (\sigma_c > 4.78) \quad (12)$$

in which ε_c^{vp} denotes the critical viscoplastic deformation, and σ_c is the creep load at a material point. For $\sigma_c < 2$ MPa (2 MPa is the tensile strength of salt), we consider that microscopically, grains remain intact and damage has not initiated, while macroscopically, material stays in the secondary creep regime.

Heat transportation and distribution of heat is controlled by a heat diffusion equation and the first law of thermodynamics, as follows:

$$\rho c_p \frac{\partial T}{\partial t} - \nabla \cdot (k \nabla T) = \dot{q}_v \quad (13)$$

in which ρ is the salt density, c_p is salt heat capacity, k is the thermal conductivity, and \dot{q}_v is the volumetric heat flux.

2.3. Model calibration

In previous studies (Zhu et al., 2015; Zhu et al., 2016), we calibrated and verified model input parameters against experimental results acquired from both short-term and long-term steady-state creep tests (Fuenkajorn and Phueakphum, 2010). The calibration process depends on both steady and tertiary states. Table 1 summarizes all parameters for the adopted damage evolution law. Table 2 presents the thermal parameters used in this simulation.

Table 1. Model parameters calibrated and verified for the exponential damage evolution law based on long-term creep test data (Fuenkajorn and Phueakphum, 2010).

Input parameter	A (day ⁻¹)	n_1 (-)	B (day ⁻¹)	n_2 (-)	χ (-)
Value	1.06e-5	4.04	1e-8	6.9	115

Table 2. Salt thermal parameters (Beardsmore and Cull, 2001; Leuger et al., 2012).

Input parameter	k (Wm ⁻¹ K ⁻¹)	c_p (Jkg ⁻¹ K ⁻¹)	α_T (K ⁻¹)
Value	7	880	4.0e-5

3. FINITE ELEMENT MODEL OF GEOLOGICAL STORAGE IN A SALT CAVERN

We implemented the phenomenological models presented above into POROFIS, a Finite Element Method (FEM)-based program developed to model coupled flow and deformation in porous fractured media (Pouya, 2015). In POROFIS, the rock stiffness in each finite element is updated at each time increment, evolving from C_0 to C_D , which allows assessing the damage effect on the stress and strain fields around the cavern.

The cavern model is axisymmetric, the cavity has a total height of 110 m (depth between 600 and 710 m) and a diameter of 100 m, similar to the cavern shape designed by Leuger et al. (2012). These types of salt caverns are usually located in bedded salt layers or areas where geological anomalies are almost unavoidable at such a shallow depth. Because of the lower in situ stress state and lower initial rock mass temperature, pressure change rates that can be sustained by a shallow cavern are lower than in a deep cavern. The salt formation has a unit weight of $\gamma = 0.02 \text{ MN/m}^3$, a Young's modulus of 23 GPa and a Poisson's ratio of 0.3 (Fuenkajorn and Phueakphum, 2010). Like in our previous study (Zhu et al., 2015), we extracted a domain of 510 m by 500 m in proximity to the salt cavern (Fig. 2), which has been checked to eliminate the boundary effect. The overburden is represented by a vertical stress of $P_V = \gamma z = 8 \text{ MPa}$ at the top boundary. To achieve an initial homogeneous in situ stress field, we applied a lateral stress of $P_H = 8 \text{ MPa}$ and an initial gas storage pressure of $P_G = 8 \text{ MPa}$ in the cavern. We fixed the vertical displacement at the bottom of the domain and the radial displacement at the left side along the axis of symmetry. Compression (respectively tension) is counted negative (respectively positive) in this study.

To estimate the temperature changes in the gas within the studied storage regime, we used the temperature data (Leuger et al., 2012) obtained from the "Salt Cavern Thermal Simulator" (SCTS) model (Nieland, 2004), which was developed to simulate the thermodynamic performance and heat transfer resulting from storage operations of a natural gas storage cavern. The SCTS model requires the input of gas composition, gas injection temperature, gas pressure cycle, and the cavern geometry characterized by the volume-to-surface-area ratio. For simplification, we assumed a uniform temperature distribution throughout the compressed gas. Pressurization and depressurization-induced temperature variation is also uniform in the cavern.

Initially, the surrounding primary rock mass temperature T_R is assumed to be 291 K. To ensure thermal equilibrium, the initial gas temperature in the cavern (T_G) is the same as the far field temperature (291 K).

Gas injection and withdrawal processes will change the gas temperature according to the SCTS model, causing a thermal gradient effect on the vicinity of the cavern.

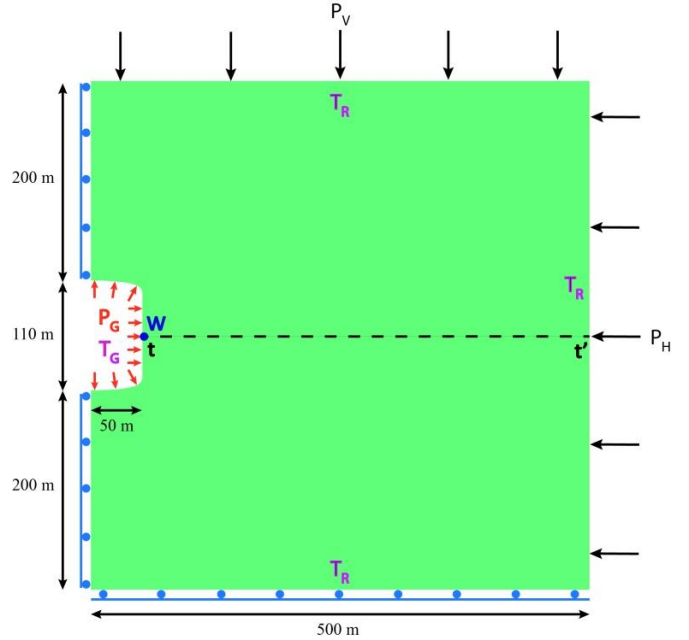


Fig. 2 Geometry and boundary conditions of the salt cavern problem, configured in GiD and studied using POROFIS. tt' is the cutting line for the observation of spatial evolution of temperature. Element W is located in the middle of the vertical cavern wall.

4. NUMERICAL STUDY OF VISCOUS DAMAGE AROUND THE SALT CAVERN

Following typical CAES conditions, we designed two stress paths sharing the same total duration of 500 days and the same gas pressure range of 5 to 8 MPa (Fig. 3).

The first stress path (O-A₁-A₂ in Fig.3) is a depressurization process and consists of three consecutive stages:

Stage 1 (at O, steady state, time-independent process): Initial in situ stress, cavern pressure and homogeneous temperature fields are applied: $P_V = P_H = P_G = 8 \text{ MPa}$, $T_R = T_G = 291 \text{ K}$.

Stage 2 (OA₁, transient state, time-dependent process): In-situ stress $P_V = P_H = 8 \text{ MPa}$ and rock mass temperature $T_R = 291 \text{ K}$ are maintained, whereas the cavern is depressurized by $\Delta P_G = -3 \text{ MPa}$ in 1 day, causing a simultaneous reduction of cavern temperature $\Delta T_G = -12 \text{ K}$.

Stage 3 (A₁A₂, transient state, time-dependent process): In-situ stress $P_V = P_H = 8 \text{ MPa}$, rock mass temperature $T_R = 291 \text{ K}$. The reduced cavern pressure $P_G = 5 \text{ MPa}$ is maintained for 499 days. This is equivalent to the idle time, which refers to phases when no gas flow occurs.

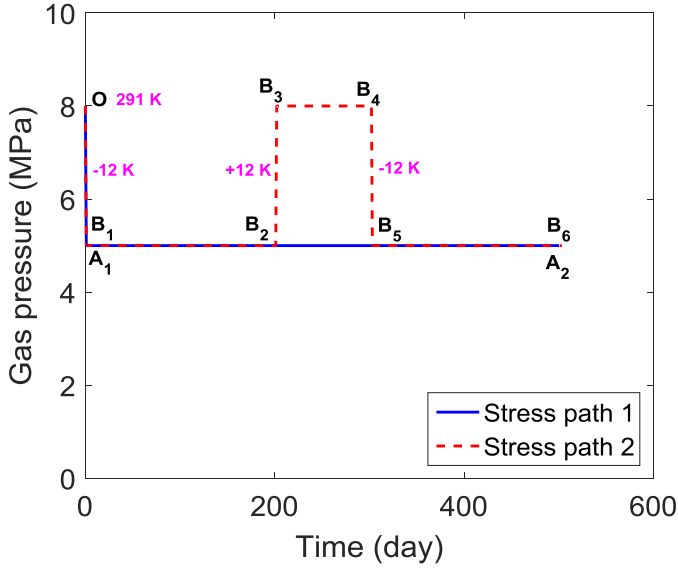


Fig. 3 Storage gas pressure and gas pressure-induced immediate temperature variations in the cavern for two thermo-mechanical stress paths.

The second stress path (O-B₁-B₂-B₃-B₄-B₅-B₆ in Fig.3) comprises a loading cycle in addition to the first loading path explained above. It can be decomposed in 7 stages, stage 1 being time-independent (steady state) and all the other stages being time-dependent (transient state). Stage 1 (O) and stage 2 (OB₁) are the same as in the first stress path. Stage 3 (B₁B₂) lasts for 199 days (instead of 499 days in the first loading path). In stage 4 (B₂B₃), the compressed gas pressure is restored in 1 day to $P_G = 8$ MPa and the temperature is increased correspondingly by $\Delta T_G = +12$ K. The high pressure storage in stage 5 is maintained for 99 days (B₃B₄) before being reduced to 5 MPa in stage 6 again within 1 day (B₄B₅). The final pressure was maintained at 5 MPa for 199 days in stage 7 (B₅B₆).

For the first stress path, we tracked the model evolution and compared radial stress, vertical stress, and temperature at the end of stage 2 and stage 3 (Fig. 4). The distributions of radial and vertical stresses are relatively homogeneous around the cavern immediately after depressurization (Figs. 4a and 4c). Viscous deformation and thermal strain considerably affect the originally homogeneous stress field, and induce significant stress concentrations at the vicinity of the cavern (Figs. 4b and 4d). In response to the gas withdrawal and consequent pressure drop, at the end of stage 2, the gas temperature decreases to 279 K at the cavern wall (Fig. 4e). Since the depressurization process is fast, the surrounding rock mass temperature remains at 291 K. At the end of 500 days of pressurization, due to the heat diffusion from the neighboring domain into the cavern, the gas temperature increases to 290.14 K and can ultimately reach the primary rock mass temperature, given sufficient time (Fig. 4f). The spatial evolution of temperature along the cutting line tt' (Fig. 2) reveals that

thermal effects are negligible beyond 50-m away from the center of the cavern (Fig. 5).

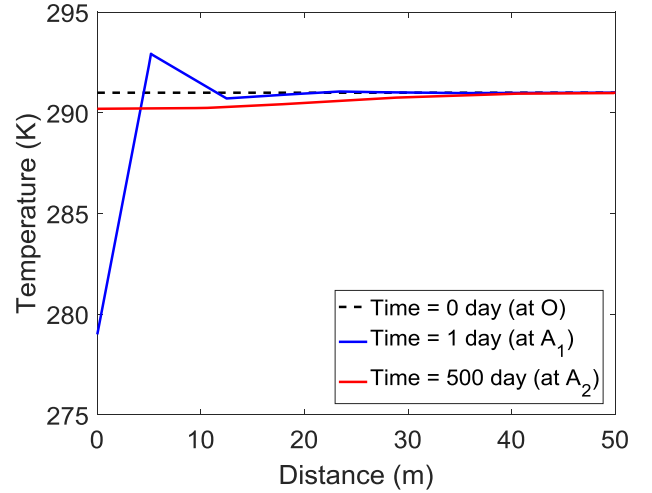


Fig. 5 Spatial evolution of temperature along the cutting line tt' at different stages in the first stress path.

The distribution of equivalent von Mises stress around the cavern after 500 days is shown in Fig. 6. Although the internal gas pressure is uniform on the cavern wall (5 MPa), we observe stress discontinuities, with high stress concentrations at the most concave sections of the cavern (Fig. 6), which is consistent with the radial and vertical stress distributions (Figs. 4b and 4d). Tracking the damage evolution shows that the cavern remains undamaged upon depressurization and damage only starts to originate and develop after entering the creep stage (A₁A₂).

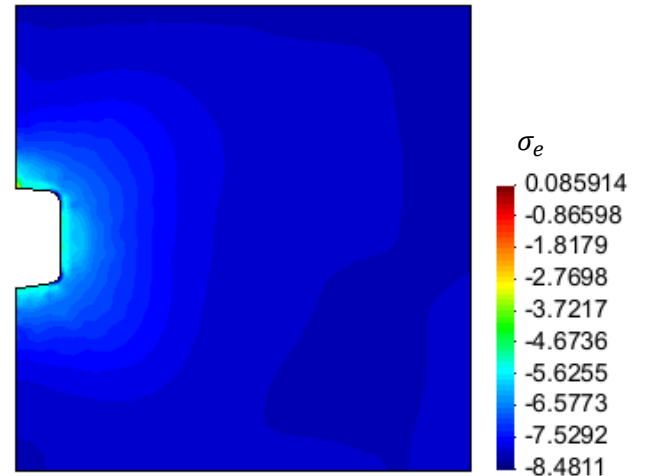


Fig. 6 Equivalent von Mises stress distribution at the end of stress path 1.

Damage distribution predicted by the damage evolution law in Eq. (9) matches well with the distribution of equivalent von Mises stress: damage reaches its maximum along the vertical cavern wall, close to the most concave part of the cavity (Fig. 7). This is consistent with the observations made in our previous study (Zhu et al., 2015): the highest accumulations of

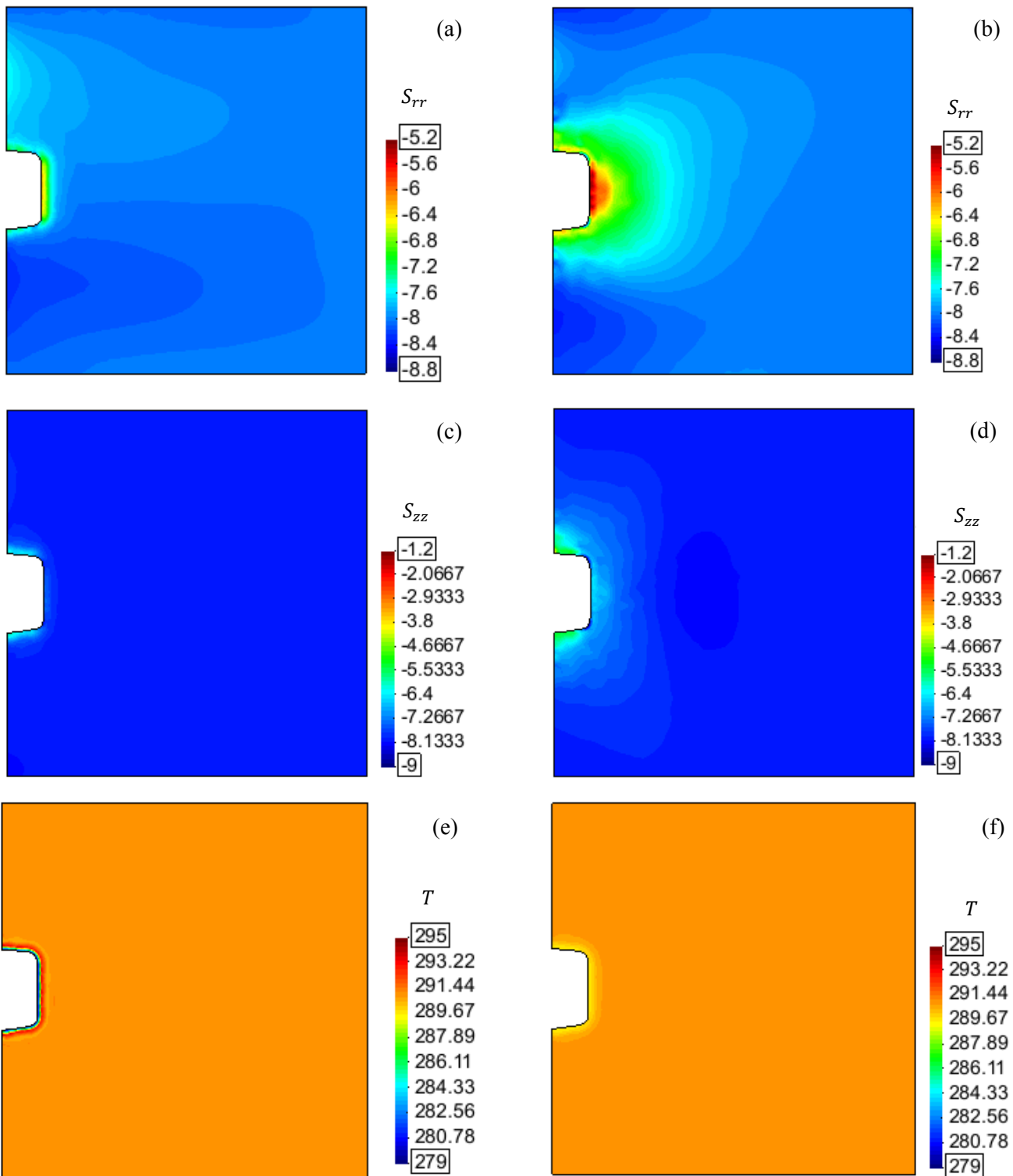


Fig. 4 Comparison of stress (in MPa) and temperature (in K) fields obtained at the end of stage 2 and stage 3 in the stress path 1: (a) radial stress at A₁, (b) radial stress at A₂, (c) vertical stress at A₁, (d) vertical stress at A₂, (e) temperature field at A₁, and (f) temperature field at A₂.

damage are found at the most irregular geometrical sections of a cavern. This analysis shows that, although damaged to a small extent at the wall, caverns for long-term storage should be carefully assessed and designed

and the applied storage pressure range should be properly monitored.

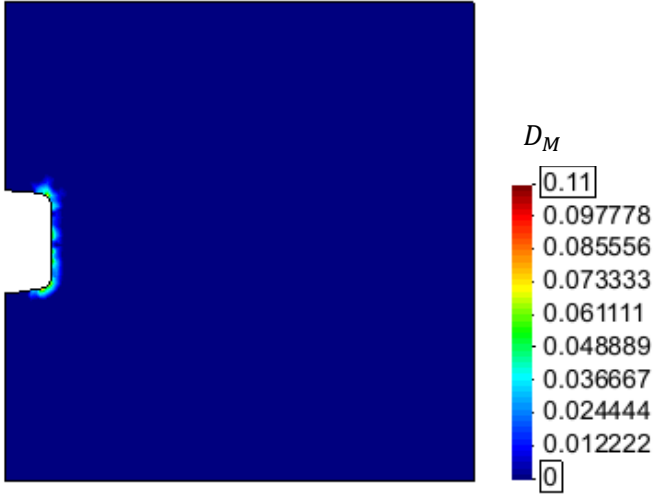


Fig. 7 Damage distribution at the end of stress path 1.

The second stress path represents a situation in which both pressurization and depressurization occur within a given period of time. At the end of stage 3 (B_1B_2), internal gas temperature undergoes a restoring period and tends to reach the ambient rock mass temperature of 291 K. The fast pressurization operation in stage 4 (B_2B_3) heats up the gas to a temperature of 301 K, much higher than the ambient temperature value (Fig. 8). 99 days of pressurization (B_3B_4) allows the cavern temperature to get close to 291 K again before the second depressurization process (B_4B_5) further cools off the gas. A similar restoring process occurs during the last stage of pressurization (B_5B_6). The ultimate temperature distributions obtained from both stress paths are almost the same, suggesting that temperature distribution always tends to reach its equilibrium with the surrounding rock mass temperature and is primarily governed by the total duration of the restoration periods: Given sufficient time, gas temperature returns to the temperature of the surround rock mass.

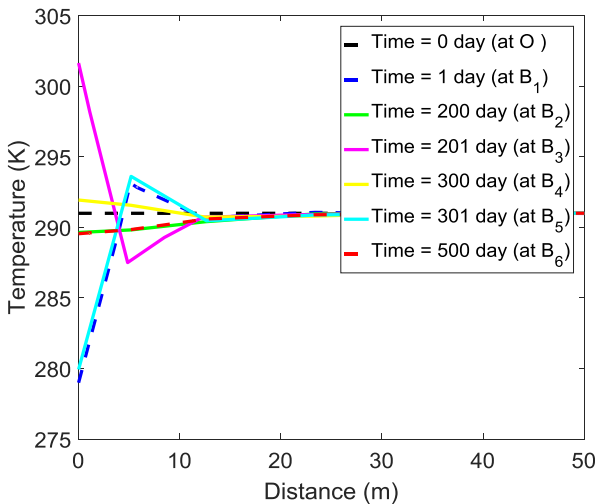


Fig. 8 Spatial evolution of temperature along the cutting line tt' at different stages in the second stress path.

Distributions of radial and vertical stresses at the end of the second stress path are also similar to those resulting from the first stress path (Figs. 4b and 4d). The damage distribution is also similar, with slightly higher damage at the corner of the salt cavern in stress path 2 (Fig. 9). This is caused by slightly higher irreversible strains and stress concentrations induced by thermo-mechanical couplings during the high pressurization stage (B_3B_4). Parametric studies also reveal that lower level of depressurization (2.5 MPa) or less stress variations enhances the stability of the rock cavern, even for an extremely long period (2000 days) of pressurization, which is conform to the simulation results obtained by Leuger et al. (2012).

These results also confirm that the idle time influences stress, strain and temperature states in the vicinity of the cavern. Idle time should be accounted for to choose the allowable pressure range of the storage facility and design cavern operations. Temperature and damage evolutions at element W (Fig. 2) in the middle of the cavern wall are shown in Fig. 10 and Fig. 11. Up to stage 3 (B_1B_2), temperature during the second stress path is similar to that during the first stress path. Although instant temperature changes occur due to gas injection and withdrawal, temperature at the vicinity of cavern tends to approach the far field temperature (Fig. 10). According to Fig. 11, damage in element W follows a similar evolution for the two stress paths considered, up to stage 4 of the second stress path. In stage 5 (B_3B_4), the cavern undergoes high pressurization while the surrounding salt formation is subjected to the same internal and in-situ stresses. The deviatoric stress decreases, which decreases also the potential to reach the damage threshold. As a result, damage stops increasing during stage 5 of the second stress path. After depressurization, damage evolution in the second stress path resumes: damage increases at approximately the same rate as in the first stress path, and remains at a lower level than damage obtained during stress path 1 throughout the remainder of the simulation. Note that results obtained at element W are not sufficient to assess the full damage zone around the caverns. For instance, even if damage reached in element W is lower in stress path 2 than in stress path 1, Fig. 7 and 9 indicate that the highest damage concentrations are obtained in stress path 2. Therefore, to further compare the influence of two stress paths, we checked the volume average of the damage variable for both stress paths, denoted as \bar{D} , which can be computed as:

$$\bar{D} = \frac{\sum_{i=1}^n D_i A_i}{\sum_{i=1}^n A_i} \quad (14)$$

in which D_i and A_i represent the damage variable and the surface area of the i^{th} element, respectively. The average damage calculated for the first stress path is 3.17×10^{-5} , and it decreases slightly to 2.87×10^{-5} for the

second stress path. For the two cases we simulated, stress path 1 with a longer constant pressurization period seems more critical. Future studies are needed to examine the effects of frequency, amplitude, and idle time of thermo-mechanical injection-withdrawal cycles on the cavern stability.

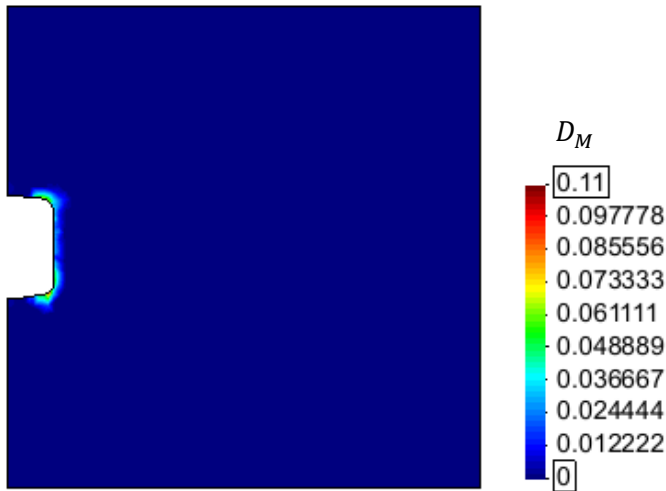


Fig. 9 Damage distribution at the end of stress path 2.

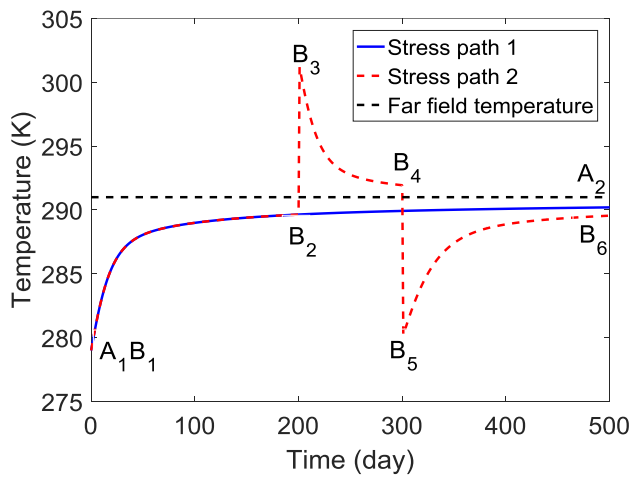


Fig. 10 Temperature evolution at element W located in the middle of the cavern side wall.

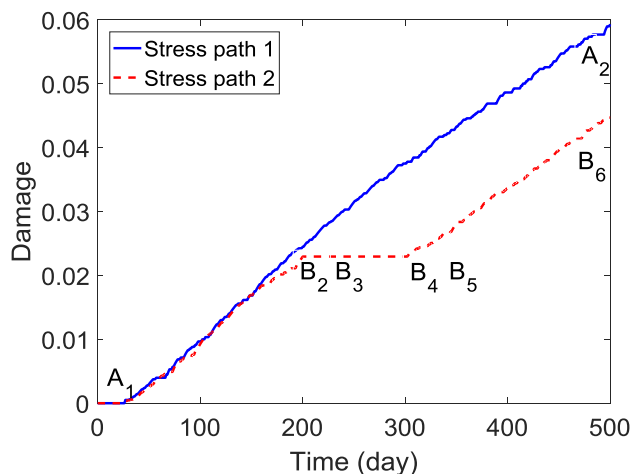


Fig. 11 Damage evolution at element W located in the middle of the cavern side wall.

5. CONCLUSIONS

The transition between secondary and tertiary creep in salt is determined by using a micro-macro model: the initiation of grain breakage is correlated with the acceleration of viscoplastic deformation rate and with the initiation of damage at the macroscopic scale. The tertiary creep law follows a similar form as the secondary creep law, but incorporates a phenomenological damage variable to account for the accelerated strain rate. We used a bilinear damage threshold to capture the transition between secondary and tertiary creep laws. Salt stiffness decreases when macroscopic damage increases, which allows predicting the evolution of the damage zone around salt caverns used for geological storage. After implementing the phenomenological model into the Finite Element Method (FEM) program POROFIS, two thermo-mechanical coupled stress paths are simulated to analyze stress concentrations and viscous damage around a 650-m-deep cavern in axisymmetric conditions. The main conclusions are the following:

- (1) Viscous deformation during the idle time significantly affects the original stress field and induces significant stress concentration near the vicinity of the cavern.
- (2) Gas temperature changes after pressurization or depressurization, but due to the heat flux from the neighboring domain into the cavern, gas temperature always converges to the primary rock mass temperature over time.
- (3) Damage distribution predicted by the damage evolution law matches well the equivalent von Mises stress distribution and reaches its highest value along the vertical cavern wall, close to the most concave sections of the cavern.
- (4) Repeated pressurization and depressurization cycles could lead to higher stress concentrations and irreversible strains at the corner of cavern due to thermo-mechanical couplings.

Results reveal the significant influences of idle time, gas pressure range, and injection and withdrawal cycles on stress, strain and temperature distributions in the vicinity of the cavern. More analyses are needed to confirm the influence of thermo-mechanical cycles of pressurization and depressurization, and to design long-term cavern operations.

ACKNOWLEDGEMENT

This research was partially funded by the U.S. National Science Foundation (grant #CMMI-1362004/1361996).

REFERENCES

1. Beardsmore, G.R. and J.P. Cull. 2001. *Crustal Heat Flow: A Guide to Measurement and Modelling*. Cambridge University Press.
2. Carter, N.L. and F.D. Hansen. 1983. Creep of rock salt. *Tectonophysics*. 92(4): 275-333.
3. Chan, K.S., S.R. Bodner, A.F. Fossum and D.E. Munson. 1992. A constitutive model for inelastic flow and damage evolution in solids under triaxial compression. *Mechanics of Materials*. 14(1): 1-14.
4. Chen Z., M.L. Wang and T. Lu. Study of tertiary creep of rock salt. *Journal of Engineering Mechanics*. 123(1): 77-82.
5. Fuenkajorn K. and D. Phueakphum. 2010. Effects of cyclic loading on mechanical properties of Maha Sarakham salt. *Engineering Geology*. 112(1-4): 43-52.
6. Haupt M. 1991. A constitutive law for rock salt based on creep and relaxation tests. *Rock Mechanics and Rock Engineering*. 24(4): 179-204.
7. Kalidindi, S.R., C.A. Bronkhorst and L. Anand. 1992. Crystallographic texture evolution in bulk deformation processing of FCC metals. *Journal of the Mechanics and Physics of Solids*. 40(3): 537-569.
8. Lan, H., C.D. Martin and J.C. Andersson. 2013. Evolution of in situ rock mass damage induced by mechanical-thermal loading, *Rock Mechanics and Rock Engineering*. 46(1): 153-168.
9. Leuger, B., K. Staudtmeister and D. Zapf. 2012. The thermo-mechanical behavior of a gas storage cavern during high frequency loading. *Mechanical Behavior of Salt VII*.
10. Ma, X. and B.C. Haimson. 2016. Failure characteristics of two porous sandstones subjected to true triaxial stresses. *Journal of Geophysical Research Solid Earth*. 121(9): 6477-6498.
11. Nieland, J.D. 2004. *Salt Cavern Thermal Simulator*. Version 2.0 User's Manual.
12. Pouya, A. 2015. A finite element method for modeling coupled flow and deformation in porous fractured media. *International Journal for Numerical and Analytical Methods in Geomechanics*. 39(16): 1836-1852.
13. Pouya, A., C. Zhu and C. Arson. 2016. Micro-macro approach of salt viscous fatigue under cyclic loading. *Mechanics of Materials*. 93: 13-31.
14. Senseny, P.E., F.D. Hansen, J.E. Russell, N.L. Carter and J.W. Handin. 1992. Mechanical behavior of rock salt: phenomenology and micromechanisms. *International Journal of Rock Mechanics and Mining Sciences & Geomechanics Abstracts*. 29(4): 363-378.
15. Urai, J.L., C.J. Spiers, H.J. Zwart and G.S. Lister. 1986. Weakening of rock salt by water during long-term creep. *Nature*. 324: 554-557.
16. Yang, C., J. Daemen and J. Yin. 1999. Experimental investigation of creep behavior of salt rock. *International Journal of Rock Mechanics and Mining Sciences*. 36(2): 233-242.
17. Zheng, L., K. Kim, H. Xu and J. Rutqvist. 2016. *DR Argillite Disposal R&D at LBNL*. Lawrence Berkeley National Laboratory, Berkeley, California, United States.
18. Zhu, C., A. Pouya and C. Arson. 2015. Micro-macro analysis and phenomenological modeling of salt viscous damage and applications to salt caverns. *Rock Mechanics and Rock Engineering*. 48(6): 2567-2580.
19. Zhu, C., A. Pouya, C. Arson, J.H. Ding, F.M. Chester and J.S. Chester. 2016. Micro-mechanical analysis of salt creep tests with a joint-enriched Finite Element Model. *The 50th US Rock Mechanics/Geomechanics Symposium*.